www.sciencemag.org/cgi/content/full/science.1204132/DC1

Supporting Online Material for

The 2010 M_w 8.8 Maule Megathrust Earthquake of Central Chile, Monitored by GPS

C. Vigny,* A. Socquet, S. Peyrat, J.-C. Ruegg, M. Métois, R. Madariaga, S. Morvan, M. Lancieri, R. Lacassin, J. Campos, D. Carrizo, M. Bejar-Pizarro, S. Barrientos, R. Armijo, C. Aranda, M.-C. Valderas-Bermejo, I. Ortega, F. Bondoux, S. Baize, H. Lyon-Caen, A. Pavez, J. P. Vilotte, M. Bevis, B. Brooks, R. Smalley, H. Parra, J.-C. Baez, M. Blanco, S. Cimbaro, E. Kendrick

*To whom correspondence should be addressed. E-mail: vigny@biotite.ens.fr

Published 28 April 2011 on *Science* Express
DOI: 10.1126/science.1204132

This PDF file includes:

Materials and Methods
SOM Text
Figs. S1 to S14
Tables S1 to S4
References

S.O.M.

GPS data processing

Static data: continuous and survey

The static data collected at continuous and survey sites were processed with the GAMIT/GLOBK software[24-25]. In the first step, we reduce 24-hour sessions to daily site positions choosing the ionosphere-free combination, and fixing the ambiguities to integer values. We use precise orbits from the International GNSS Service for Geodynamics (IGS) and IGS Tables to describe the phase centers of the antennae[26]. We estimate one tropospheric vertical delay parameter per station every 3 hours. The horizontal (resp. vertical) components of the calculated relative position vectors are precise to within 1-3 (resp. 3-5) mm. In the second step, we produce daily time series by constraining regional stations unaffected by the earthquake to their well known coordinates in the ITRF2005 (essentially KOUR in French Guyana, BRAZ, BRFT and CHPI in Brasil, RIO2 in Patagonia and GLPS on the Nazca plate). Finally we estimate co-seismic jumps in two different ways for continuous or survey sites. For continuous stations it is simply the difference between the day before and the day after the earthquake. For survey sites, we determine the co-seismic displacements by extrapolating the last known position before the earthquake to the date of the re-survey after the earthquake using the inter-seismic rate, and by comparing the latest to the present positions. Those displacements are affected by higher uncertainties than those of the cGPS stations (a few mm) because an uncertainty of 1-3 mm/yr on the inter-seismic rate, will map into an uncertainty of 1-3 cm for the extrapolated position at an average date of 8 years after the 2020 survey. Since the smallest horizontal displacement of survey sites is 70 cm, this source of error is limited to 3% of the signal at most. Using the date of the earthquake rather than the date of the re-survey (carried out 2 to 3 weeks after the earthquake) to extrapolate last known positions to pre-

earthquake positions changes them by no more than 1 mm (20 days at an average velocity of 20 mm/yr). However, it is clear that post-earthquake measurements include co-seismic displacements and 2 to 3 weeks of post-seismic displacement. Coastal sites are likely to be affected by the largest post-seismic deformation: additional displacements of 10 to 15 cm after 2 to 3 weeks are detected by available cGPS stations. This is the largest source of error, but remains small (3%) relative to the magnitude of the co-seismic displacements (3 to 5 m).

High rate GPS (HRGPS) data

Epoch-to-epoch processing of the high rate GPS data (HRGPS) has been described to analyze cGPS station displacements during an earthquake[27-28]. We process the high sampling rate data (1 Hz) using the TRACK software developed at MIT. We also use the LC combination and IGS precise orbits, and apply a smoothing filter on the backward solution to estimate the atmospheric delays using the whole 24hours data and fix any non-integer biases to a constant value. Because TRACK computes a relative position with respect to a fixed reference station, we choose to use the same for all moving sites: UAPE (Iquique) of our cGPS network, with the exception of CONZ (the southernmost station) processed relative to SILL (La Silla). We picked this station because it is far enough so that surface waves which move this station arrives late enough so that the first 500s are unaffected by this motion. It is difficult to asses the accuracy of HRGPS in general. Some low frequency biases related to atmosphere drift or satellite configuration changes may show, depending on the length of the baseline to the reference station. This does not affect the co-seismic step since it is an almost instantaneous displacement, but renders difficult the chase for pre-seismic or rapid post-seismic signal. Performance of given receiver types also play a role: some lost lock on several satellites for a few seconds (CONZ, SANT), some several times during the earthquake. Different processing techniques will handle differently those short periods with less or no data.

Aliasing in these relatively low frequency data (compared to 100 Hz seismograms) is usually present and described as a problem for earthquake source studies with motograms[29].

However, the aliasing problem is the worst for medium size events whose energy spectrum peaks near the Nyquist frequency (0.5 Hz for 1 Hz sampling). In this particular case, the energy in the high pass filtered acceleration data (the signal that produces aliasing) has an amplitude that is the same order of magnitude as the energy in the low pass filtered acceleration data. As the earthquake gets bigger (and Maule is much bigger), the peak of the energy spectrum moves to lower frequencies (it does not loose energy at the higher frequencies, but the amplitude of this signal is a smaller percentage of the total amplitude and becomes unimportant. For Maule, we are also farther away from the fault, the minimum in this case is the depth to the fault under the station. But we are farther from the epicenter than in Smalley's study (3 km). The earth is a good low pass filter and the high frequencies will get attenuated over short distances. In addition, GPS itself is also a good low pass filter: if one uses 5 mm as the resolution of HRGPS (and not 1mm like Smalley), this further reduces the effect of aliasing as most of the aliased signal is below the resolution of HRGPS. So there might be some aliasing during some portion of the record. But it should not significantly affect the result, and does not prevent from identifying seismic waves and picking up phases like we simply do.

Relative land level change

Along the coast, natural or anthropogenic markers also depict the co-seismic vertical displacements of the crust relative to the sea level. Such displacements have been estimated in different places along the rupture zone from field geological survey and testimonies, and from comparison of pre and post-earthquake satellite imagery and photographs. A critical review of available data, including ours, suggests that uncertainties are often of several tens of centimeters, thus implying that vertical displacements lower than ~50 cm are difficult to assess safely. Substantial subsidence is detected North of Constitución for at least 80 km along the coast (zone in blue on Fig. 2b). Near Caleta La Pesca (site 2 Fig. 2b), pre and post

earthquake high-tide lines can be identified on inundated meadows and rock outcrops. There, preliminary measurements suggest a conservative estimate of at least 1 m of subsidence (possibly up to 2 m). 10 km North, at Caleta Duao (site 1 Fig. 2) we estimated between 80 cm and 160 cm of subsidence in the fishing harbor again from tide levels. Last is a breathtaking testimony from a fisherman that was collecting clams offshore La Trinchera (site 3 on Fig 2) with seawater to the knees when he felt the earthquake and suddenly lost ground and had to swim to save his life, likely as a result of metric co-seismic subsidence. On the opposite, clear evidence of uplift are found West of Concepcion, along the coasts of Tumbes and Hualpén peninsulas (e.g., Caleta Chome, site 4 Fig 2, 60-80 cm of uplift measured from comparison of high-tide lines). More to the South, field evidence of strong uplift are clear along the coast of the Arauco peninsula South of Caleta Lavapié (site 5 Fig 2) for at least 80 km (e.g., at Caleta Rumena or Lebu). At Caleta Lavapié, for instance, we measured ~2 m of uplift on the pier (here also from comparison of high-tide lines). Given the uncertainties, these estimates of vertical displacement and their regional pattern are fully compatible with GPS results and give additional constraints North of Constitución where GPS results are sparse (Fig. 2b).

Elastic modeling and inversion

The surface deformation fields associated with the co- and post-seismic phases are modeled using Okada's formulation of a dislocation buried in an infinite elastic half space[30]. The fault geometry is constrained by the trace of the trench at the surface. We assume a uniform dip of 15° and a variable rake, so that the direction of slip is constant at all patches. The fault is discretized into an array of 25 × 15 elements, measuring approximately 30km × 18km. This geometry is used to invert for the slip distribution using a compilation of available displacement data for the co-seismic slip, coastal land-level variations and Alos Wide Swath interferogram released on UNAVCO supersite, and our 12 days of post-earthquake GPS displacement field for the post-seismic slip solution. To solve for the slip distribution along the 375 patches of the fault, we use a least-squares minimization with a non-negativity

constraint on the slip. Slip is forced to zero at the edges of the fault (including at the trench). To limit oscillations of the solution, we impose smoothing by minimizing the second-order derivative of the fault slip. We determine the optimal solution roughness that will be used in our final models searching for a compromise between the roughness and the misfit of the solution. We explore a series of different values for the slip azimuth (rake). The N83° azimuth that best fits the data corresponds to a rake of 116° where the trench strikes N19°, which exactly fits the slip obliquity deduced from the CMT focal mechanism and makes an angle of ~5° with the plate convergence azimuth (N77°). InSAR data is down-weighted and represent 7% only of the total weight of the inverted data. Therefore, InSAR data helps constrain the slip distribution where we lack GPS data, but has almost no influence where we have dense GPS measurements. The roughness of the preferred co-seismic distribution is 0.26 cm/km. The L2-norm of misfit (rms) is 15.4 cm to the InSAR data, and 10.75 cm to GPS and land-level variation data. Our co-seismic model reduces the variance by 97.08%. For the post-seismic slip distribution, the preferred roughness is 0.00533 cm/km for a rms of 0.55 cm to the cGPS data and a variance reduction of 99.91%.

Modeling of the HRGPS: synthetics motograms

We computed synthetics motograms (Fig. 4) using a modified version of the Axitra program[31]**.** The velocity and density structure was obtained from a local study[32]. We found that rupture speeds between 2.8 and 3.1 km/s produce good fit between synthetics and observed motograms, and we used 3.1 km/s for all synthetics shown. We tested many published models and selected the slip model determined from static data presented in this work. This model fits all the static components accurately so that it fits the near field stations very well, except for the NS component of the motogram at CONS. We improved the fit by fixing the azimuth of the slip vector to N87°, and used the dip and strike of the static GPS model shown in Figure 3. By trial and error, we chose the rise time at every point of the fault using a triangular source time function of 20s duration. We computed the least squared fit of

the synthetics to the observed motograms. The synthetics reduce the variance of the original data by more than 98%. This is much better than the variance reductions obtained in usual seismic source inversion using strong motion data. The reason is that the EW displacements at CONS and CONZ are much larger than the other components, and larger than motograms at all other stations so that the usual L2 measure of fit becomes insensitive to details in the wave form.

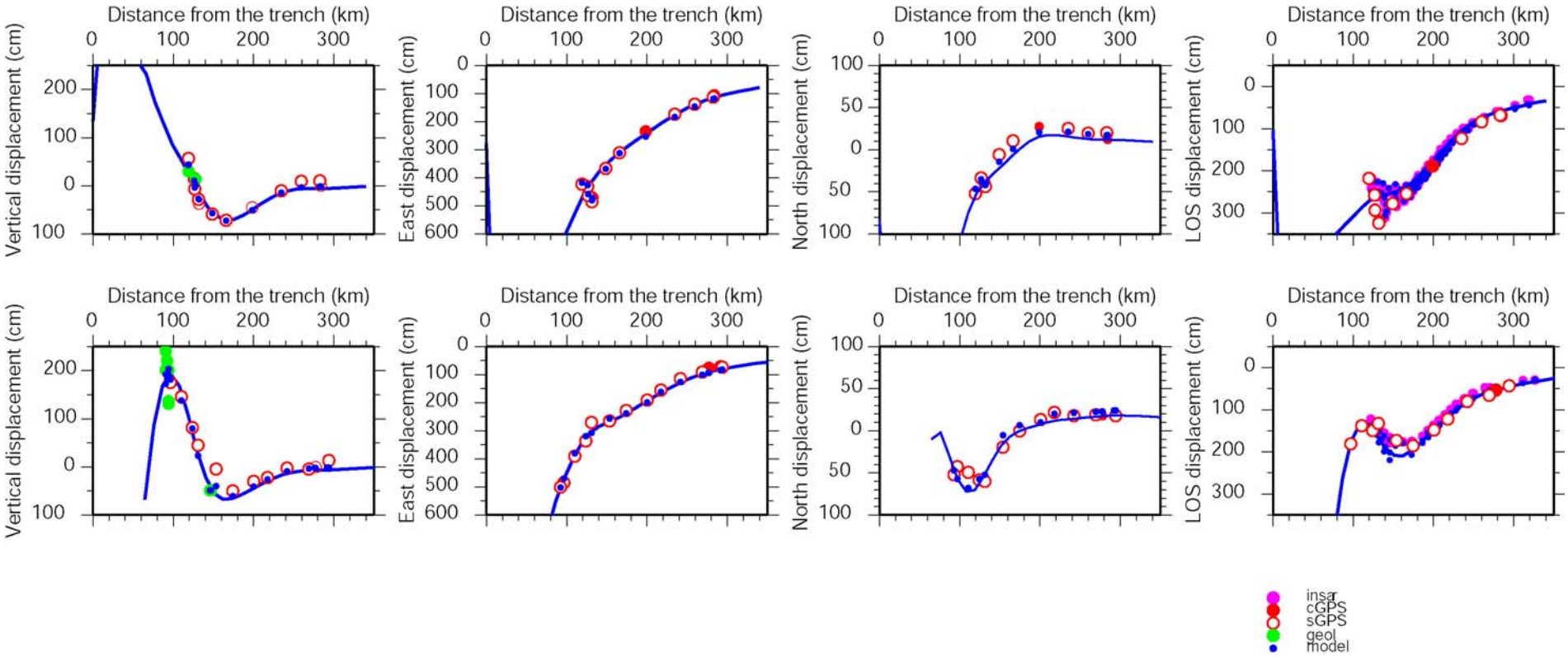

Fig. S1 Cross section of displacements against distance to trench. The two cross sections correspond to the two dashed lines on Fig. 3, approximately at the latitudes of Constitucion (upper boxes) and Arauco-Concepcion (lower boxes). Data points located within 20km-width stripes centered on each profile are projected in the section plane. Different columns depict different projections of the displacements: uplift or subsidence (1st column), East-West (2nd column), North-South (3rd column) and total displacements projected in the radar line of sight (LOS) (i.e. value of digitized SAR interferogram superimposed with 3D GPS displacements projected in the satellite LOS). Green dots show relative land-level changes measured from geological markers. Red dots show GPS measurements (full for cGPS and open for sGPS). Purple dots depict InSAR deformation. Blue dots show the value of the model at the data points, and the blue line depicts the value of the model along the cross section.

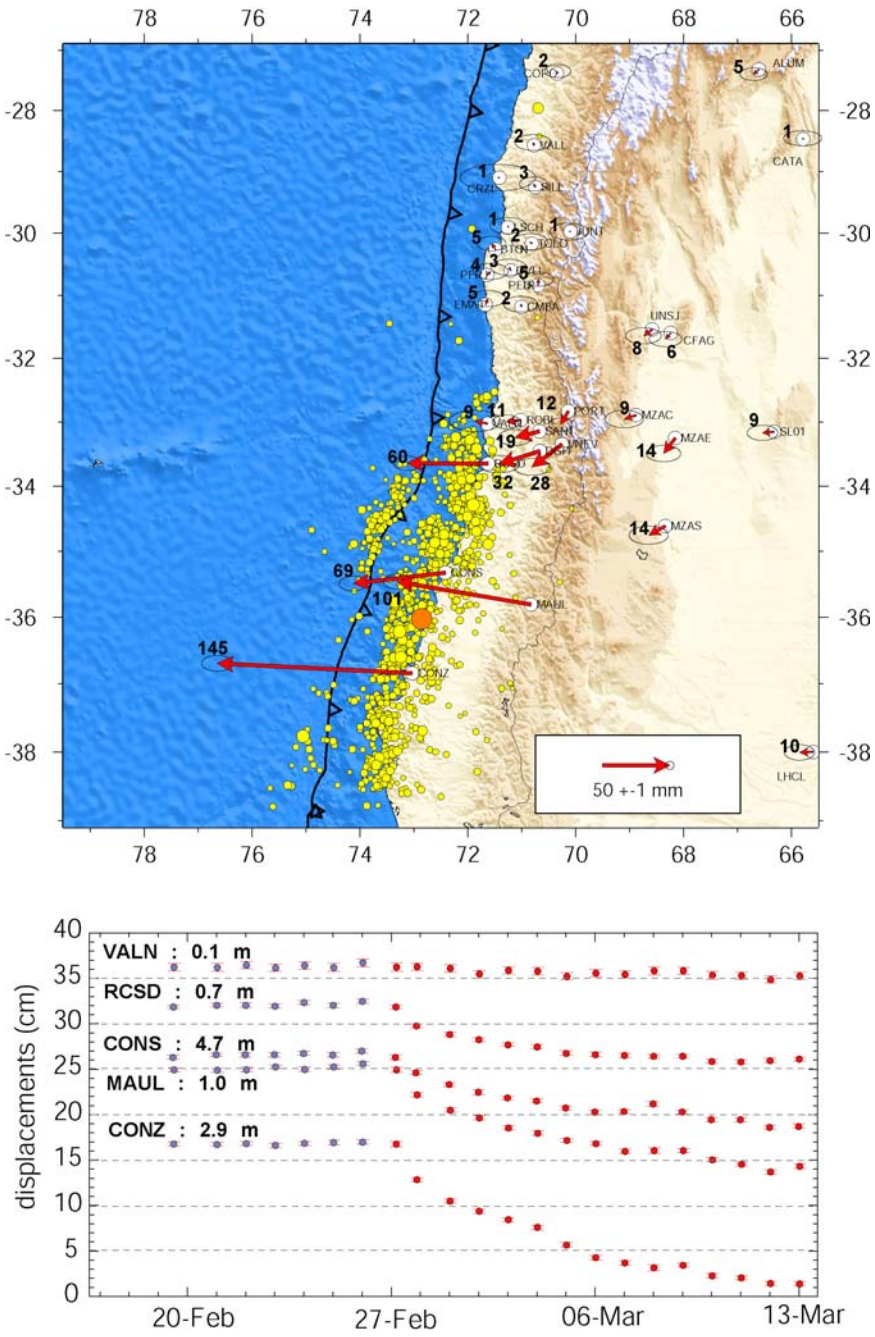

Fig. S2 Pre- and post-seismic deformation at cGPS sites. In the upper box, red vectors show the total amount of the first 12 days of post-seismic deformation. Bold numbers next to arrow heads give the displacement in mm. Ellipses depict the 99% confidence level of formal uncertainties. Other symbols are identical to those of figure 1. The lower bow shows daily time series of the eastern component at selected sites (VALN, RSCD, CONS, MAUL, CONZ), both before and after the earthquake. There is 1 dot per daily position, blue dots depict positions before the earthquake and red dots positions after the earthquake; the co-seismic jump is removed. Horizontal scale is in days, vertical scale is cm (1 dashed line every 5 cm) with an arbitrary origin.

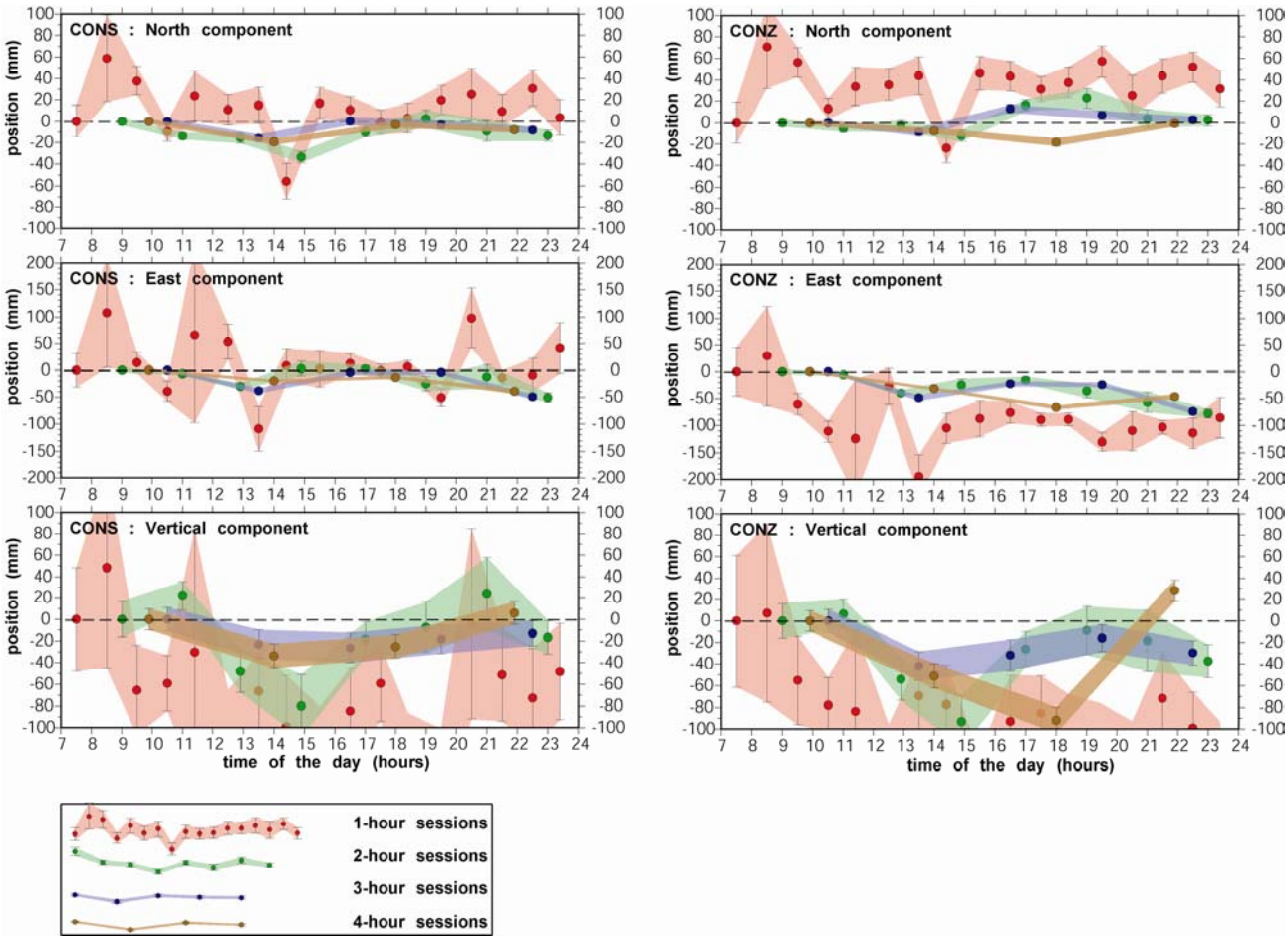

Fig. S3 Short static processing sessions of 1,2,3,4 hours of data following the earthquake at two selected sites (CONS and CONZ); North component (top), East component (middle), vertical component (bottom). Elapsed time is UTC hour of the day. Displacement scale is in mm. Uncertainties depict the 95% confidence level (3-sigma).

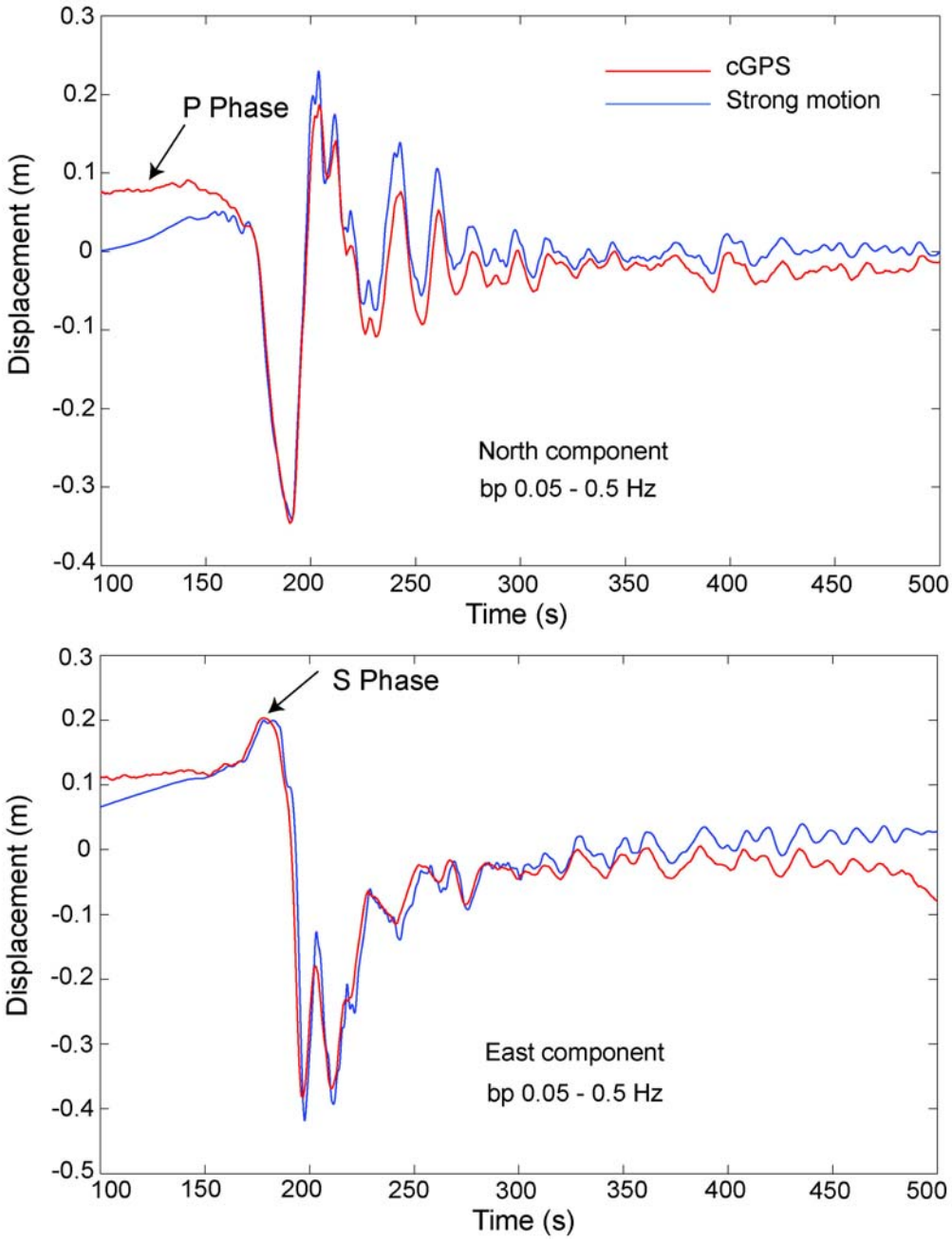

Fig. S4 Comparison of band pass filtered motograms and accelerograms recorded at the El Roble (ROBL) site. The accelerograms have been twice integrated and filtered in the frequency band from 0.02 Hz to 0.5 Hz for the North South component and from 0.02 to 0.5 Hz for the East West component. Motograms have been band pass filtered in the same frequency range. The filter was a non-causal Buttersworth filter with 4 poles. 0.5 Hz is the Nyquist frequency of the motograms.

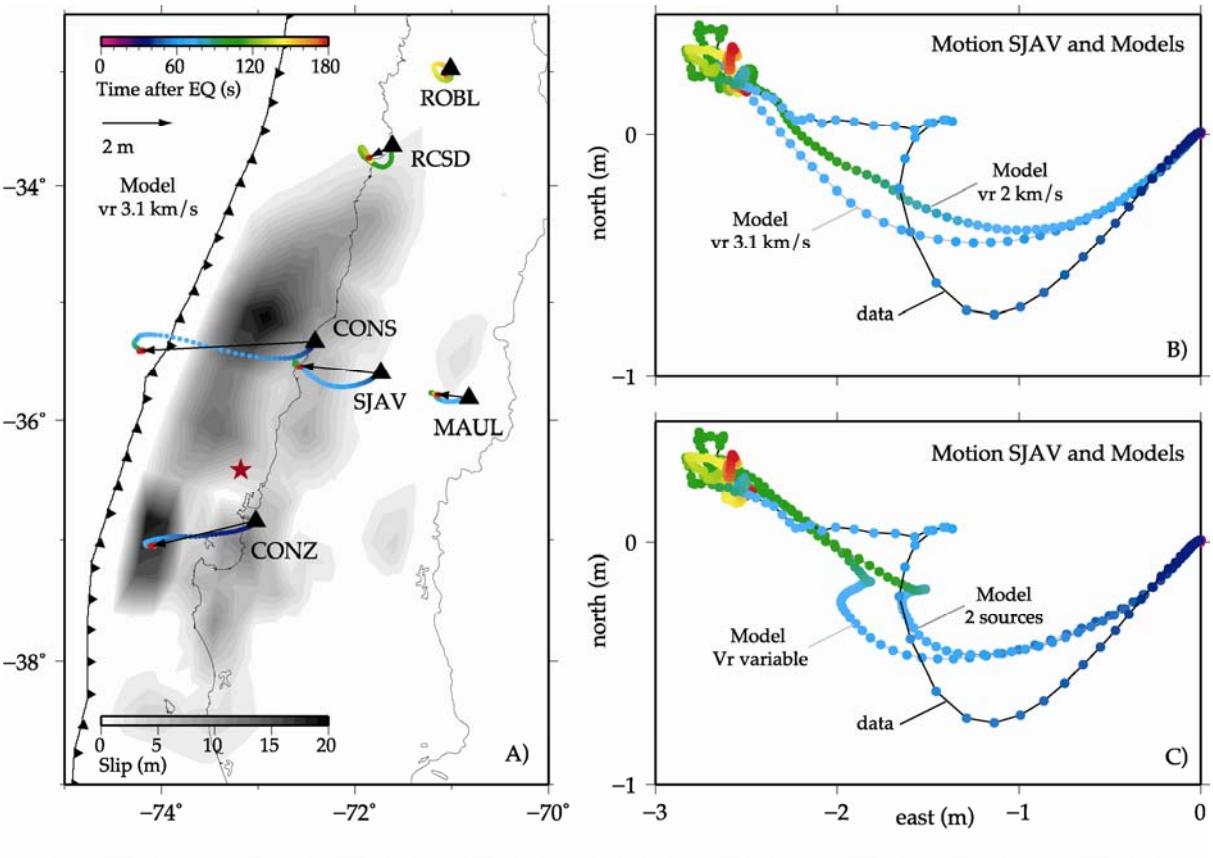

Fig. S5 Near field motograms, particle motions and details at SJAV. The left box (A) shows cGPS sites synthetic color coded particle motion computed with a simple source model: a simple dislocation propagating radially away from the epicenter at 3.1 km/s. The total slip is the one of our best fit model presented in Fig. 3. Black vectors represent the static displacement for this model, and the red star is our hypocenter. The upper right box (B) shows observed and synthetic particle motion curves at San Javier (SJAV). Two constant velocities are displayed: Vr=3.1 km/s and Vr = 2km/s. Overall, a velocity of 3.1 km/s reproduces well the cGPS data (i.e. the timing of the total displacement) but fails to reproduce details of the station displacement (i.e. the "kink" at 60s). A velocity of 2 km/s is too slow and it takes twice the observed time (120s instead of 60s) for the station to reach its final position. The lower right box (C) depicts the effect of rupture kinematics on surface displacements and how a variable rupture velocity may produce the observed kink at 60s. Model "Vr variable" has a deceleration and an interruption, during which the rupture is slightly delayed after 140 km of radial propagation. Model "2-sources" has a second source located 170 km north of the epicenter, from where the rupture propagates 60 seconds after the beginning of the earthquake. Both models generate a kink in the particle motion but fail to match the timing of the observed motion. Additional complexities of the source are needed.

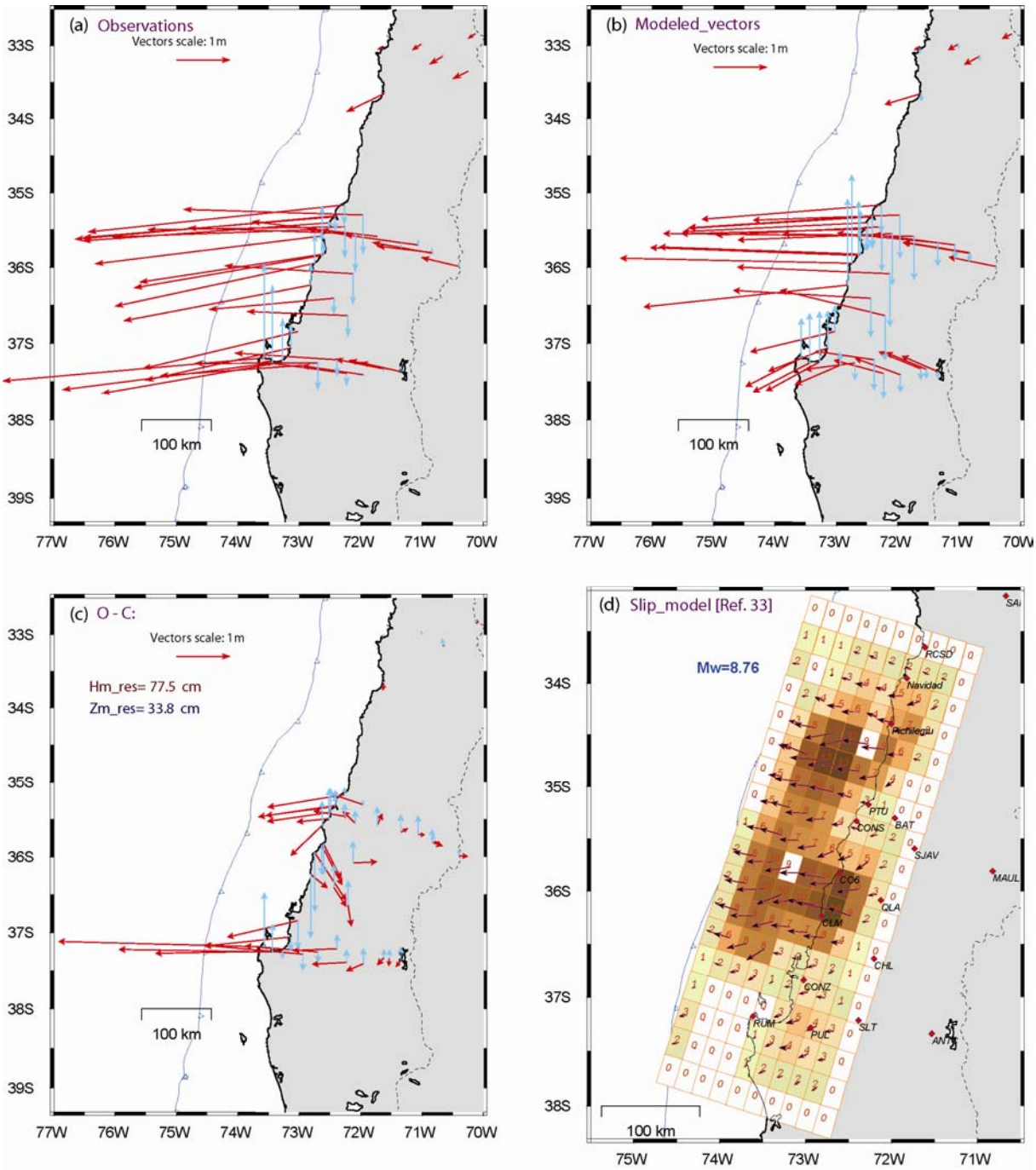

Fig. S6 Observed and computed displacement of the February 27, 2010 Mw = 8.8 Maule Earthquake, on the GPS stations from the finite-fault slip distribution of G. Hayes[33]. Observed horizontal (red) and vertical (blue) displacement vectors on the GPS networks of the Central South area of Chile (cGPS and repetition French-Chilean GPS network)

a) Computed horizontal (red) and vertical (blue) displacement vectors from the slip distribution of .Hayes. The magnitude indicated is the computed one.
b) O-C (observed-computed) vectors. The values indicated on the lower right corner are the mean residuals for horizontal and vertical vectors respectively.
c) Finite-fault slip distribution from G. Hayes (USGS) projected onto the Earth surface, with values of slip (m) indicated on each individual patches and rake directions showed by vectors.

Comment: The computed displacements are correct in amplitude and direction in the northern part of the studied area, except in the coastal area where residual have an average amplitude of 1m, but miss to match the observed deformation in the southern area of Concepcion-Arauco, because of lack of slip in the southern area of the model.

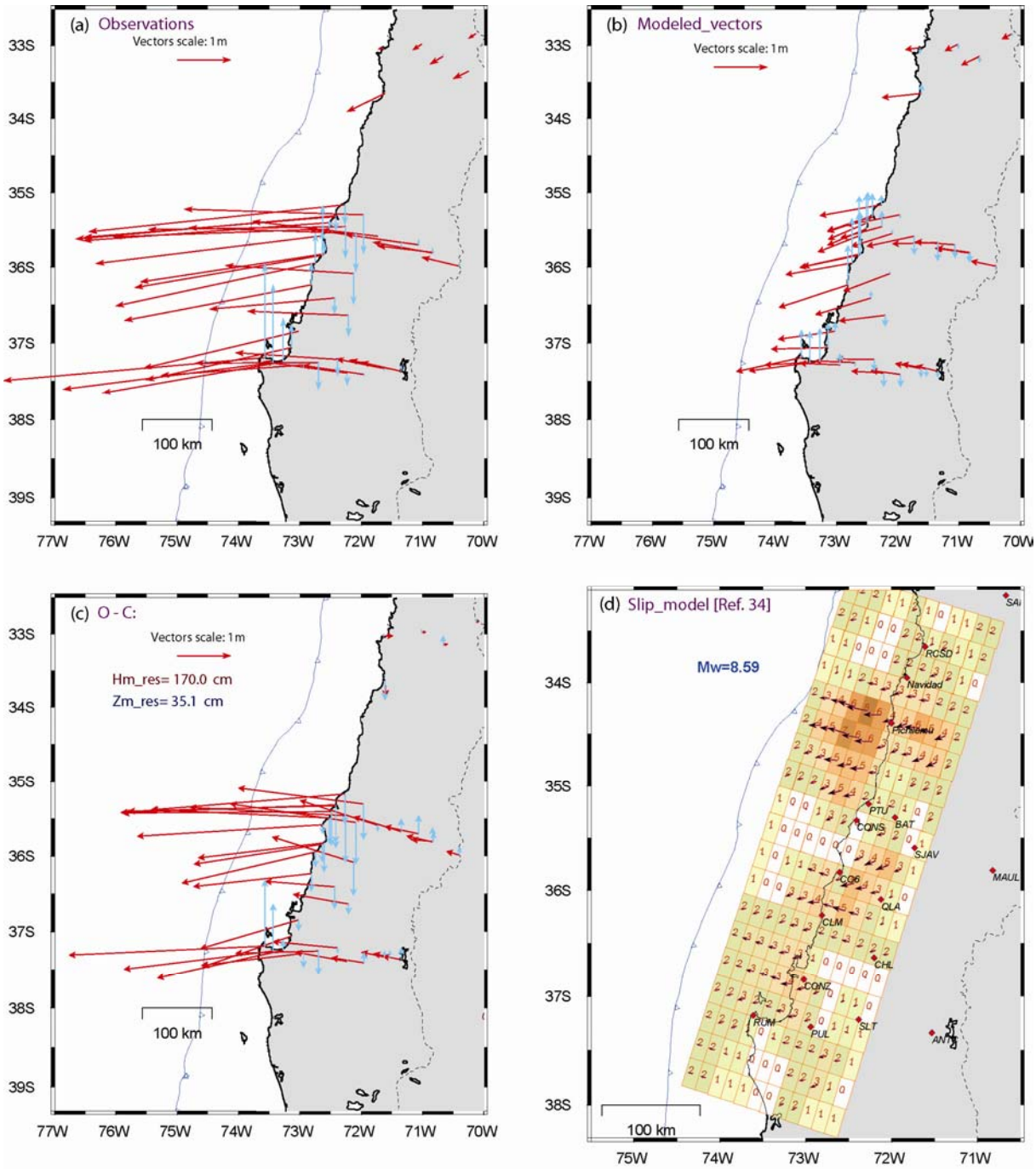

Fig. S7 Observed and computed displacement of the February 27, 2010 Mw = 8.8 Maule Earthquake, on the GPS stations from the finite-fault slip distribution of A. Sladen[34].

a) Observed horizontal (red) and vertical (blue) displacement vectors on the GPS networks of the Central South area of Chile (cGPS and repetition French-Chilean GPS network)
b) Computed horizontal (red) and vertical (blue) displacement vectors from the slip distribution of .A. Sladen. The magnitude indicated is the computed one.
c) O-C (observed-computed) vectors. The values indicated on the lower right corner are the mean residuals for horizontal and vertical vectors respectively.
d) Finite-fault slip distribution from A. Sladen (Caltech) projected onto the Earth surface, with values of slip (m) indicated on each individual patches and rake directions showed by vectors.

Comment: The computed vectors are too small with respect to the observed vectors. The computed magnitude Mw= 8.59 is also smaller than the observed one Mw=8.8, because most of the patches lack slip (maximum slip: 8.25 m and mean value: 2.3 m). On the other hand the rupture extends northward as far as Valparaiso (33°S), but our GPS observations show that its northern extension is not beyond Navidad (~Punta Topocalma 34°S). Further more, small slip values on the southern part of the rupture lead to computed displacement ~1 m in the coastal area of Arauco-Concepcion, when observed ones are larger than 4 m.

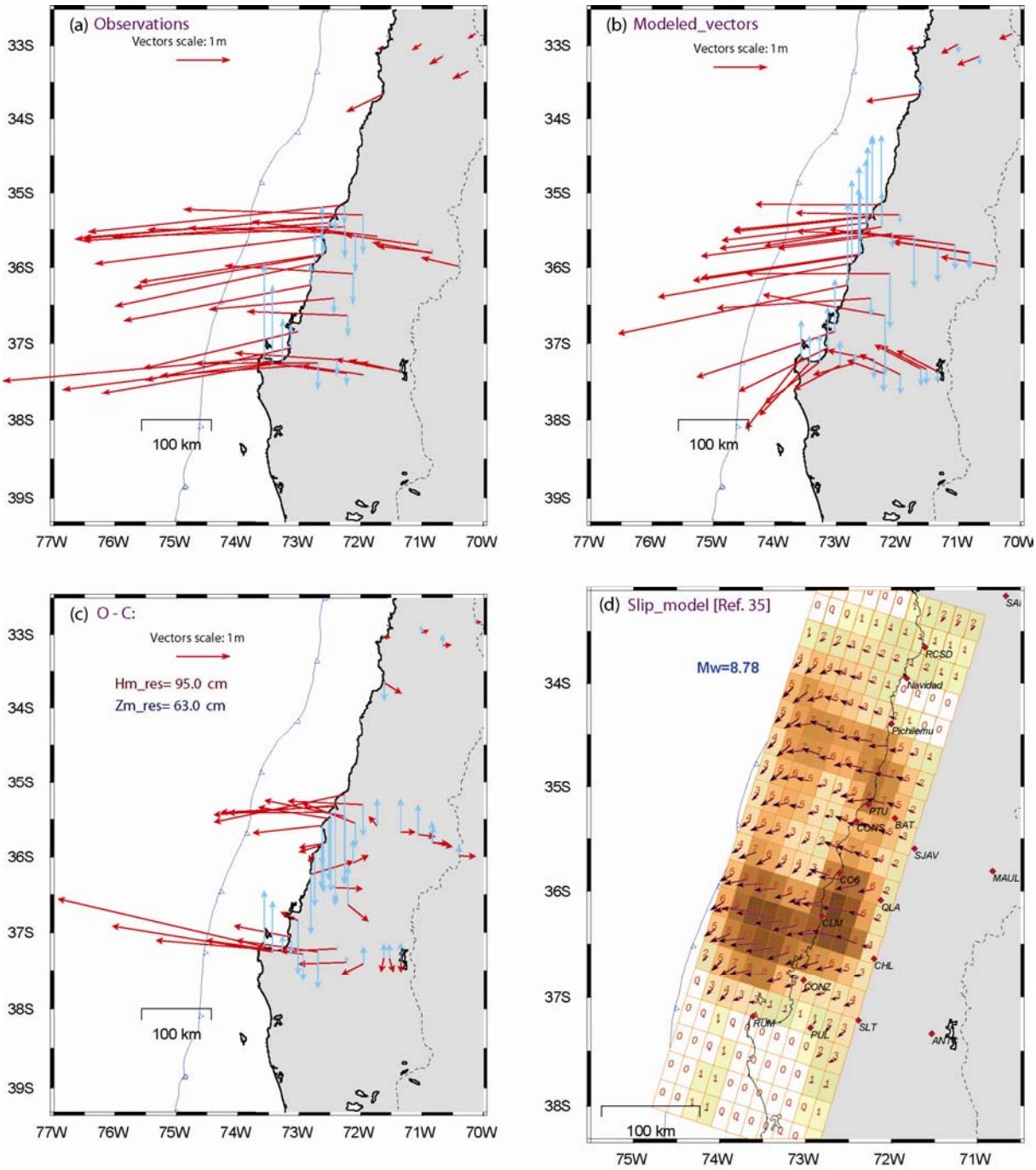

Fig. S8 Observed and computed displacement of the February 27, 2010 Mw = 8.8 Maule Earthquake, on the GPS stations from the finite-fault slip distribution of Shao et al.[35]

a) Observed horizontal (red) and vertical (blue) displacement vectors on the GPS networks of the Central South area of Chile (cGPS and repetition French-Chilean GPS network)
b) Computed horizontal (red) and vertical (blue) displacement vectors from the slip distribution of .Chen Ji. The magnitude indicated is the computed one.
c) O-C (observed-computed) vectors. The values indicated on the lower right corner are the mean residuals for horizontal and vertical vectors respectively.
d) Finite-fault slip distribution from Chen Ji (UCSB) projected onto the Earth surface, with values of slip (m) indicated on each individual patches and rake directions showed by vectors.

Comment: The computed horizontal vectors are correct in amplitude and direction in the central area between Constitucion and Concepcion, but too small elsewhere. In the Consitucion area and northwards, the computed horizontal vectors are too small and the vertical ones are positive (uplift) when observed values are negative (subsidence). Southwards, Conception area computed horizontal vectors are mis-oriented and too small of about 2-3 m. The slip distribution is concentrated north and west of Concepcion and lacks slip near Constitucion and towards the trench.

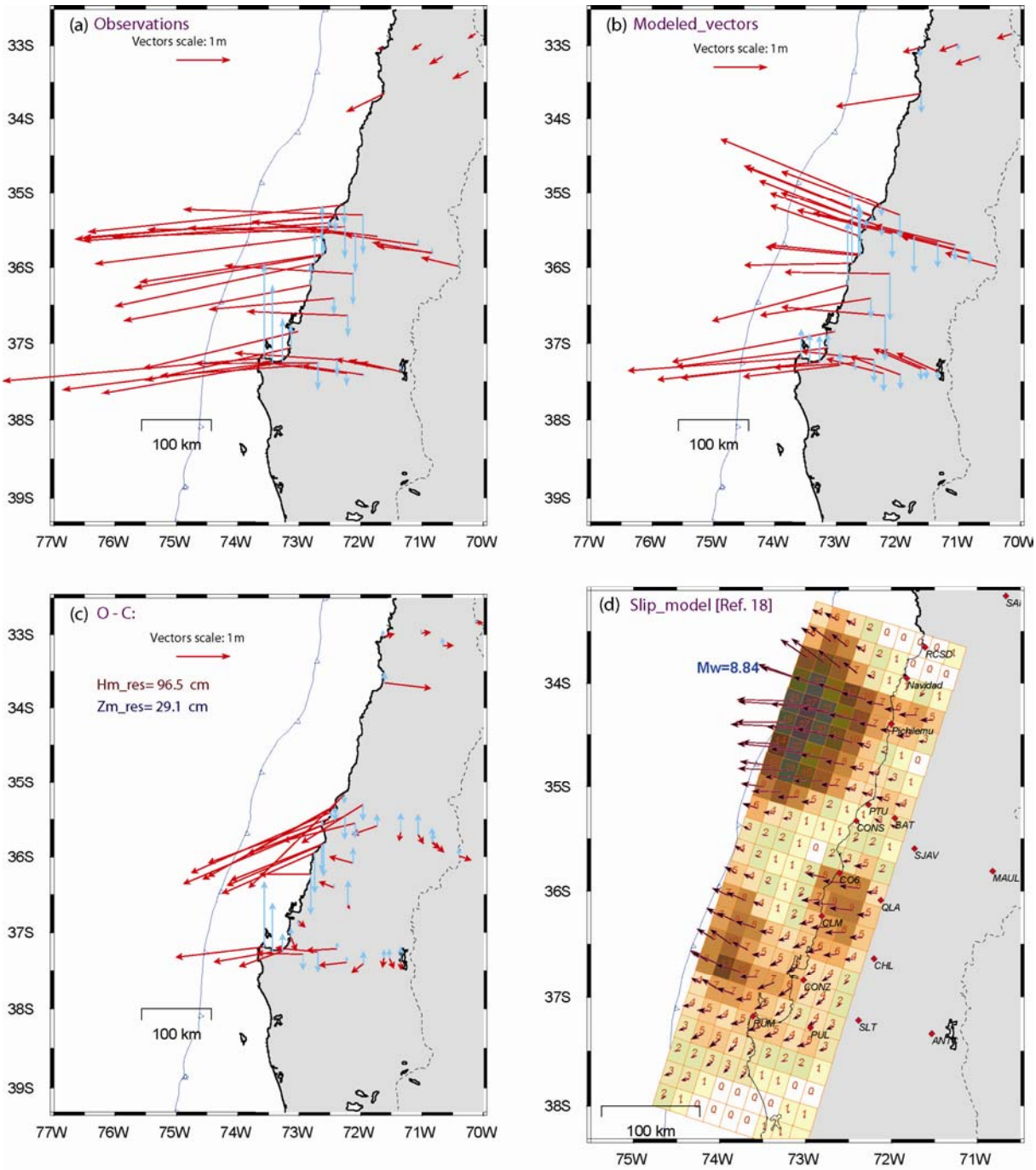

Fig. S9 Observed and computed displacement of the February 27, 2010 Mw = 8.8 Maule Earthquake, on the GPS stations from the finite-fault slip distribution of Lay et al.[18]

a) Observed horizontal (red) and vertical (blue) displacement vectors on the GPS networks of the Central South area of Chile (cGPS and repetition French-Chilean GPS network)
b) Computed horizontal (red) and vertical (blue) displacement vectors from the slip distribution of .Lay and al. The magnitude indicated is the computed one.
c) O-C (observed-computed) vectors. The values indicated on the lower right corner are the mean residuals for horizontal and vertical vectors respectively.
d) Finite-fault slip distribution from Lay and al. (2010) projected onto the Earth surface, with values of slip (m) indicated on each individual patches and rake directions showed by vectors.

Comment: This model has shallow slip near the trench. However, due to the strong concentration of very large slip (>25m) NW of Constitution and Pichilemu (34.5°S), computed horizontal vectors are too small and mis-oriented in the northern area near Constitucion. Computed vectors are better in the Concepcion area, but vertical vectors are largely underestimated in the Arauco area.

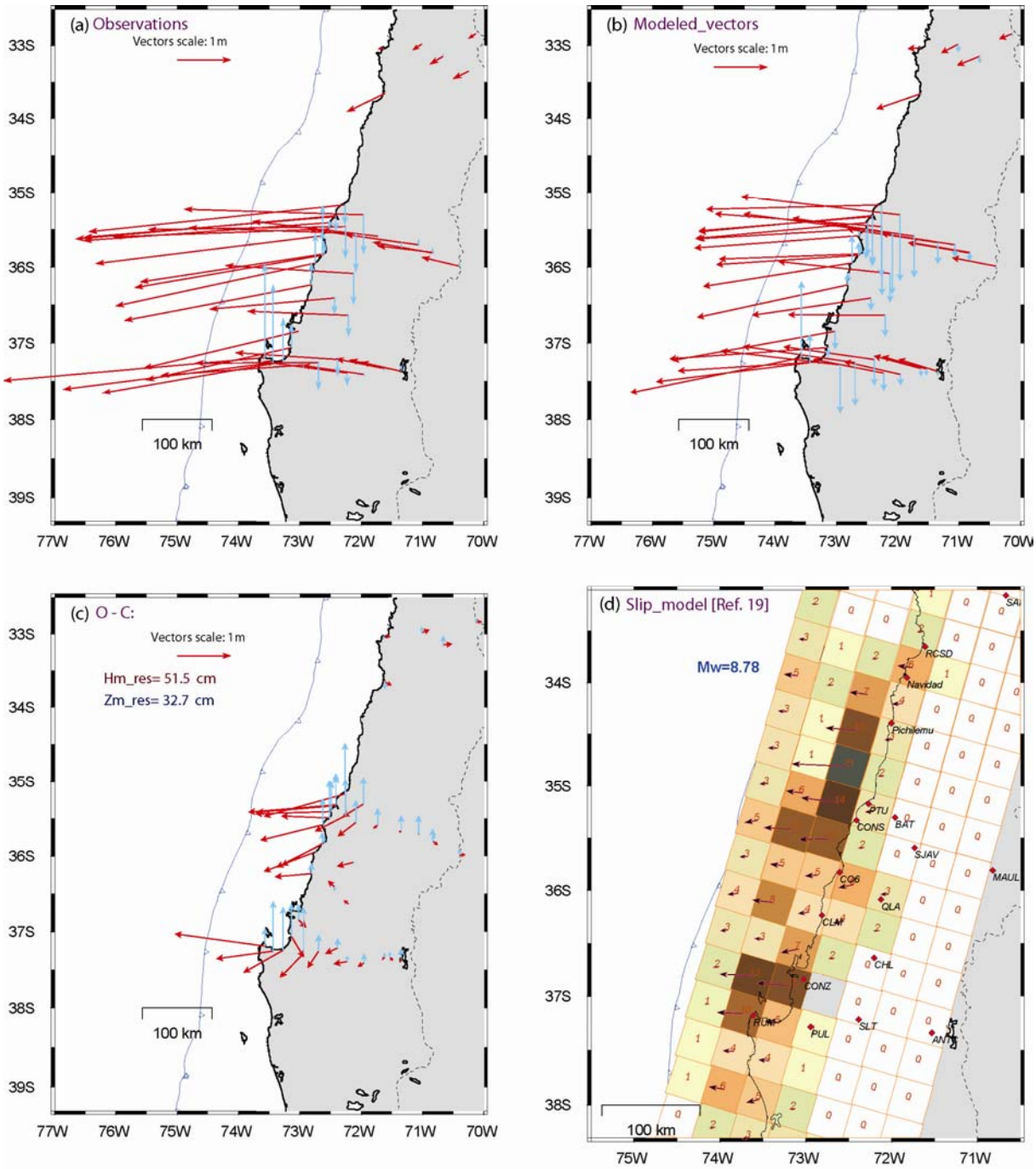

Fig. S10 Observed and computed displacement of the February 27, 2010 Mw = 8.8 Maule Earthquake, on the GPS stations from the finite-fault slip distribution of Delouis et al.[19]

a) Observed horizontal (red) and vertical (blue) displacement vectors on the GPS networks of the Central South area of Chile (cGPS and repetition French-Chilean GPS network)

b) Computed horizontal (red) and vertical (blue) displacement vectors from the slip distribution described in this paper. The magnitude indicated is the computed one.

c) O-C (observed-computed) vectors. The values indicated on the lower right corner are the mean residuals for horizontal and vertical vectors respectively.

d) Finite-fault slip distribution described in this paper projected onto the Earth surface, with values of slip (m) indicated on each individual patches and rake directions showed by vectors.

Comment: This slip model yields a better fit to observations than the previous ones, both for horizontal and vertical components. However, residuals are larger than 1 m all along the coastline between Consitucion and Arauco, probably because the model lacks shallow slip near the trench.

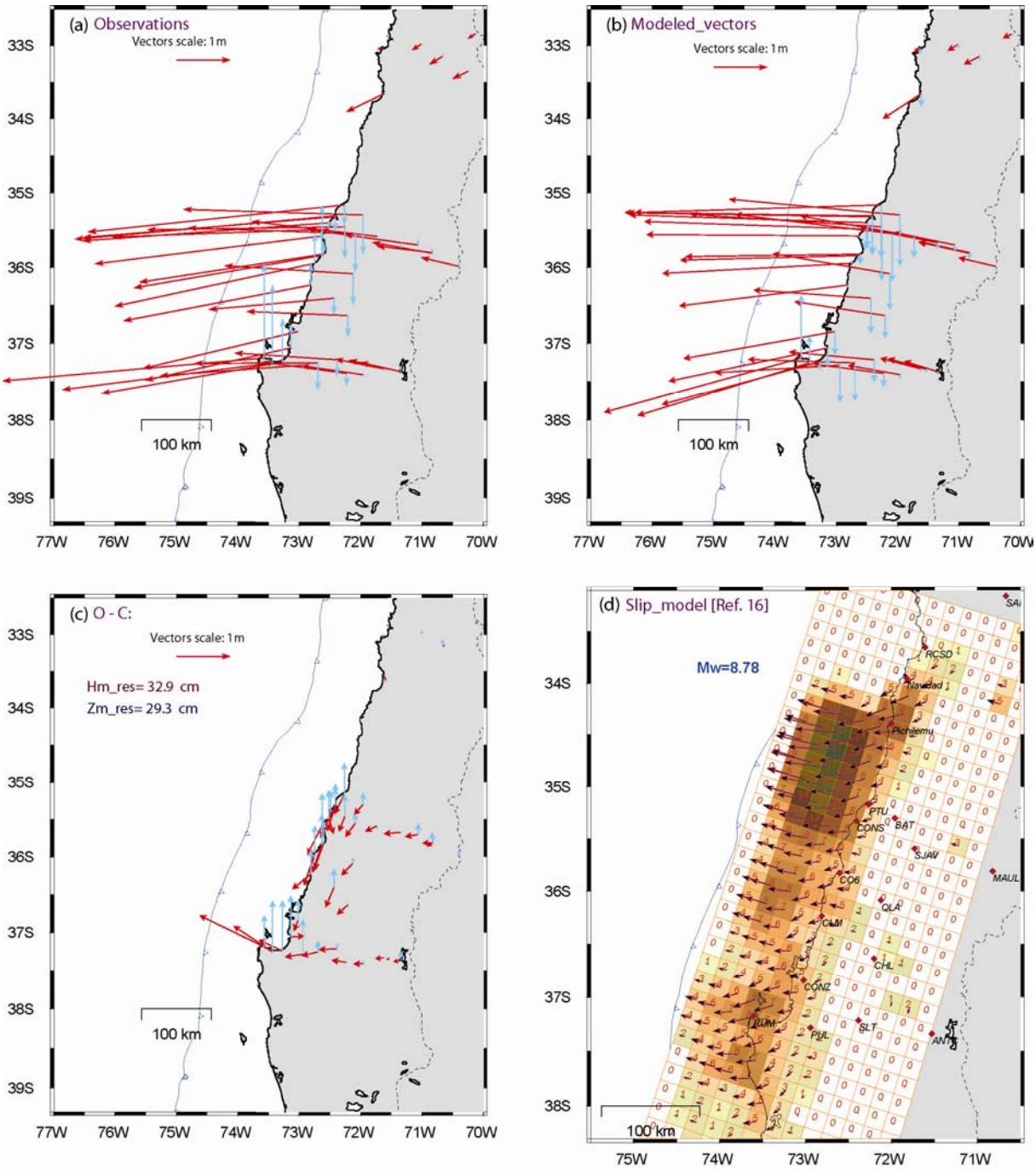

Fig. S11 Observed and computed displacement of the February 27, 2010 Mw = 8.8 Maule Earthquake, on the GPS stations from the finite-fault slip distribution of Tong et al.[16]

a) Observed horizontal (red) and vertical (blue) displacement vectors on the GPS networks of the Central South area of Chile (cGPS and repetition French-Chilean GPS network)
b) Computed horizontal (red) and vertical (blue) displacement vectors from the slip distribution described in this paper. The magnitude indicated is the computed one.
c) O-C (observed-computed) vectors. The values indicated on the lower right corner are the mean residuals for horizontal and vertical vectors respectively.
d) Finite-fault slip distribution described in this paper projected onto the Earth surface, with values of slip (m) indicated on each individual patches and rake directions showed by vectors.

Comment: This slip model has the smallest residuals with our observations. It slightly underestimates slip in the southern area near Arauco peninsula and uplift all along the coast.

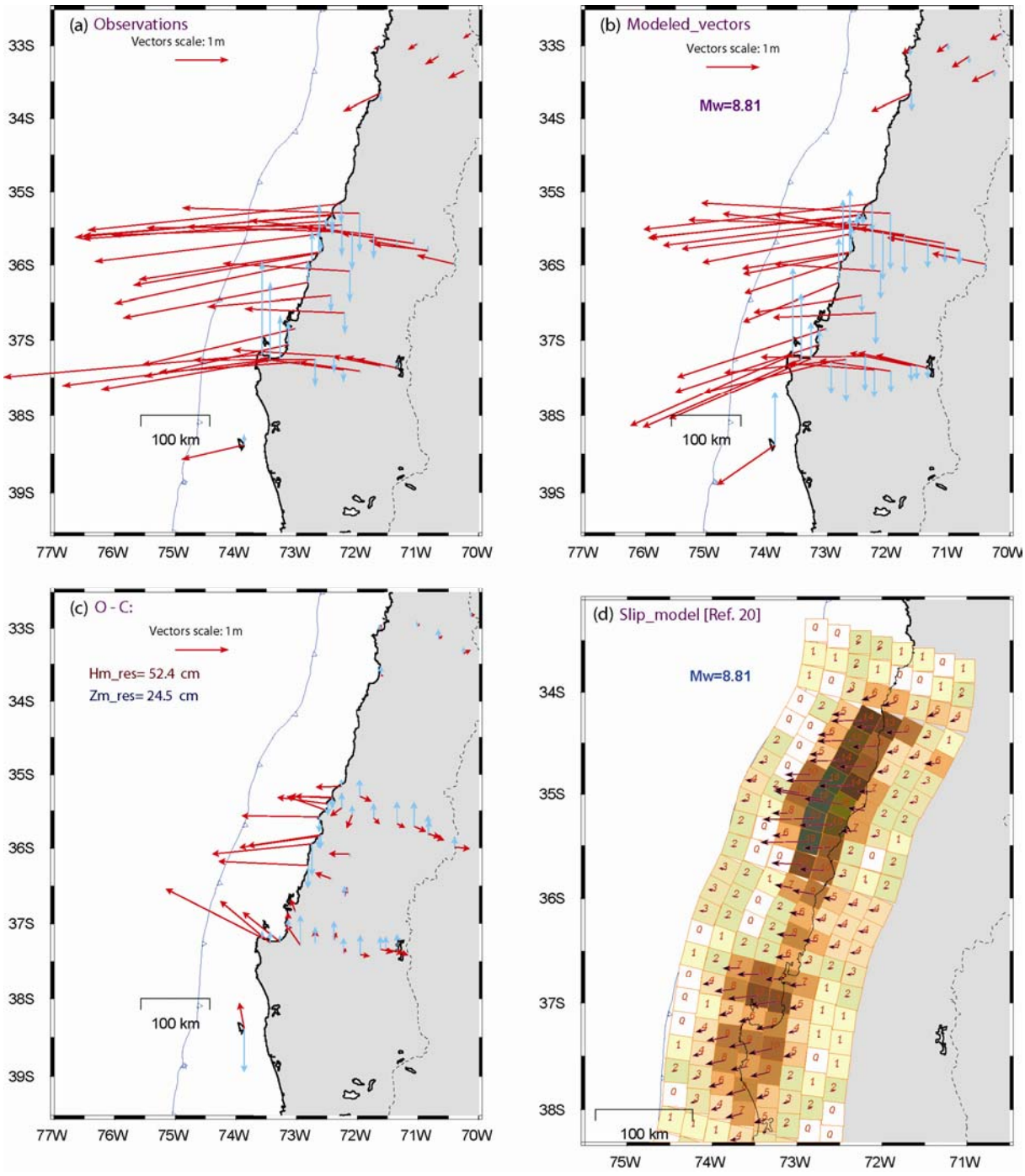

Fig. S12 Observed and computed displacement of the February 27, 2010 Mw = 8.8 Maule Earthquake, on the GPS stations from the finite-fault slip distribution of Lorito et al.[20]

a) Observed horizontal (red) and vertical (blue) displacement vectors on the GPS networks of the Central South area of Chile (cGPS and repetition French-Chilean GPS network)

b) Computed horizontal (red) and vertical (blue) displacement vectors from the slip distribution described in this paper. The magnitude indicated is the computed one.

c) O-C (observed-computed) vectors. The values indicated on the lower right corner are the mean residuals for horizontal and vertical vectors respectively.

d) Finite-fault slip distribution described in this paper projected onto the Earth surface, with values of slip (m) indicated on each individual patches and rake directions showed by vectors.

Comment: This slip model matches well the observed displacements, except along the coast where the computed vectors are systematically smaller than the observed ones (~1-2 m). Vertical subsidence is also slightly overestimated inland. Those two features are probably due to too deep localization of slip and lack of shallow slip at the trench.

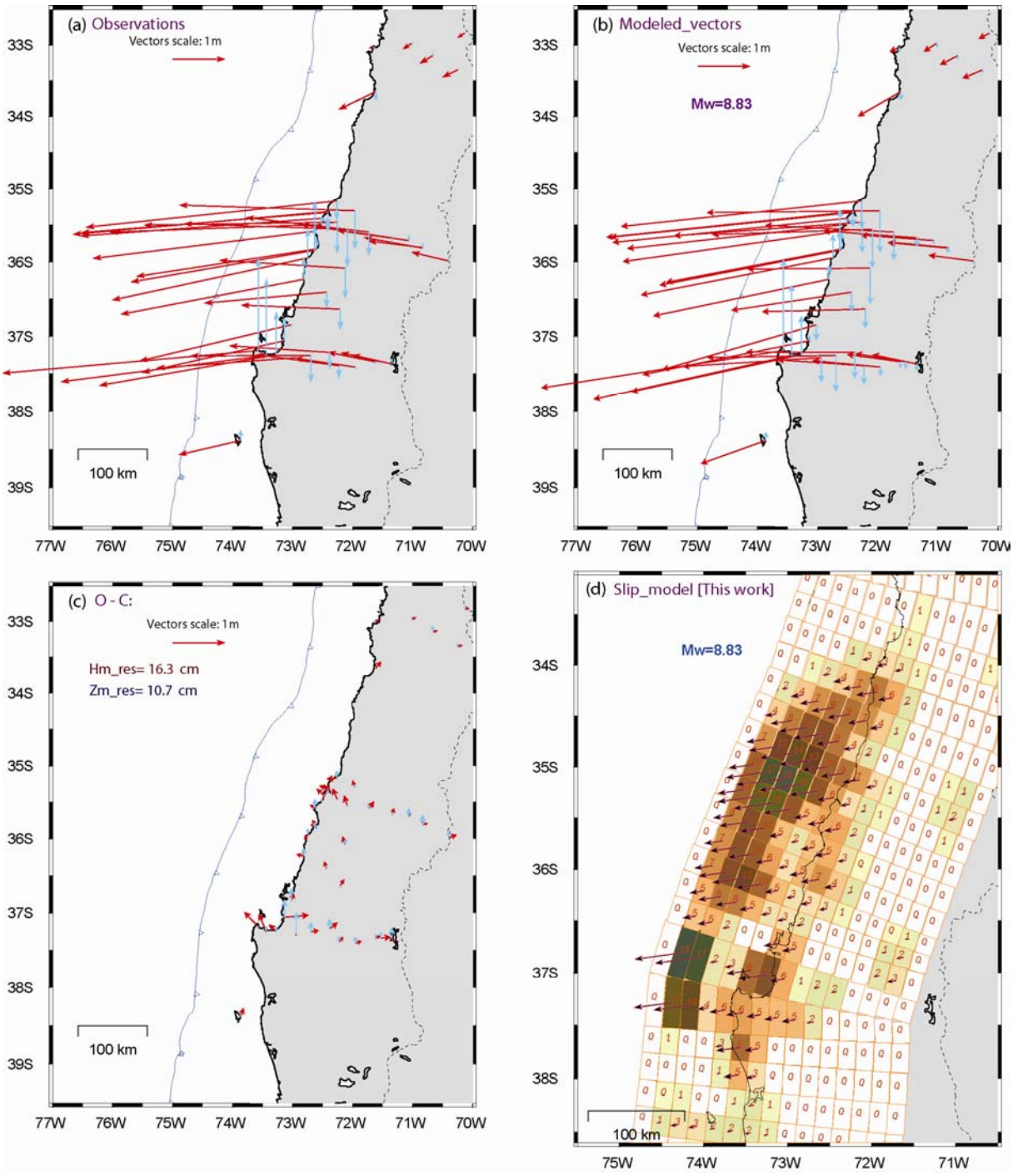

Fig. S13 Observed and computed displacement of the February 27, 2010 Mw = 8.8 Maule Earthquake, on the GPS stations from the finite-fault slip distribution of this work.

a) Observed horizontal (red) and vertical (blue) displacement vectors on the GPS networks of the Central South area of Chile (cGPS and repetition French-Chilean GPS network)
b) Computed horizontal (red) and vertical (blue) displacement vectors from the slip distribution described in this paper. The magnitude indicated is the computed one.
c) O-C (observed-computed) vectors. The values indicated on the lower right corner are the mean residuals for horizontal and vertical vectors respectively.
d) Finite-fault slip distribution described in this paper projected onto the Earth surface, with values of slip (m) indicated on each individual patches and rake directions showed by vectors.

Comment: Our final model includes the observed GPS displacements for the Mocha Island [Tong et al., 2010] and the vertical data from land level changes obtained by [Farias et al., 2010]. Therefore, the southern end of the rupture is better constrained. The computed vectors fit better the observations than those from any previous models both for horizontal and vertical components, especially near the coast, with mean horizontal residuals of about 16.3 cm and mean vertical residuals of 10.7 cm.

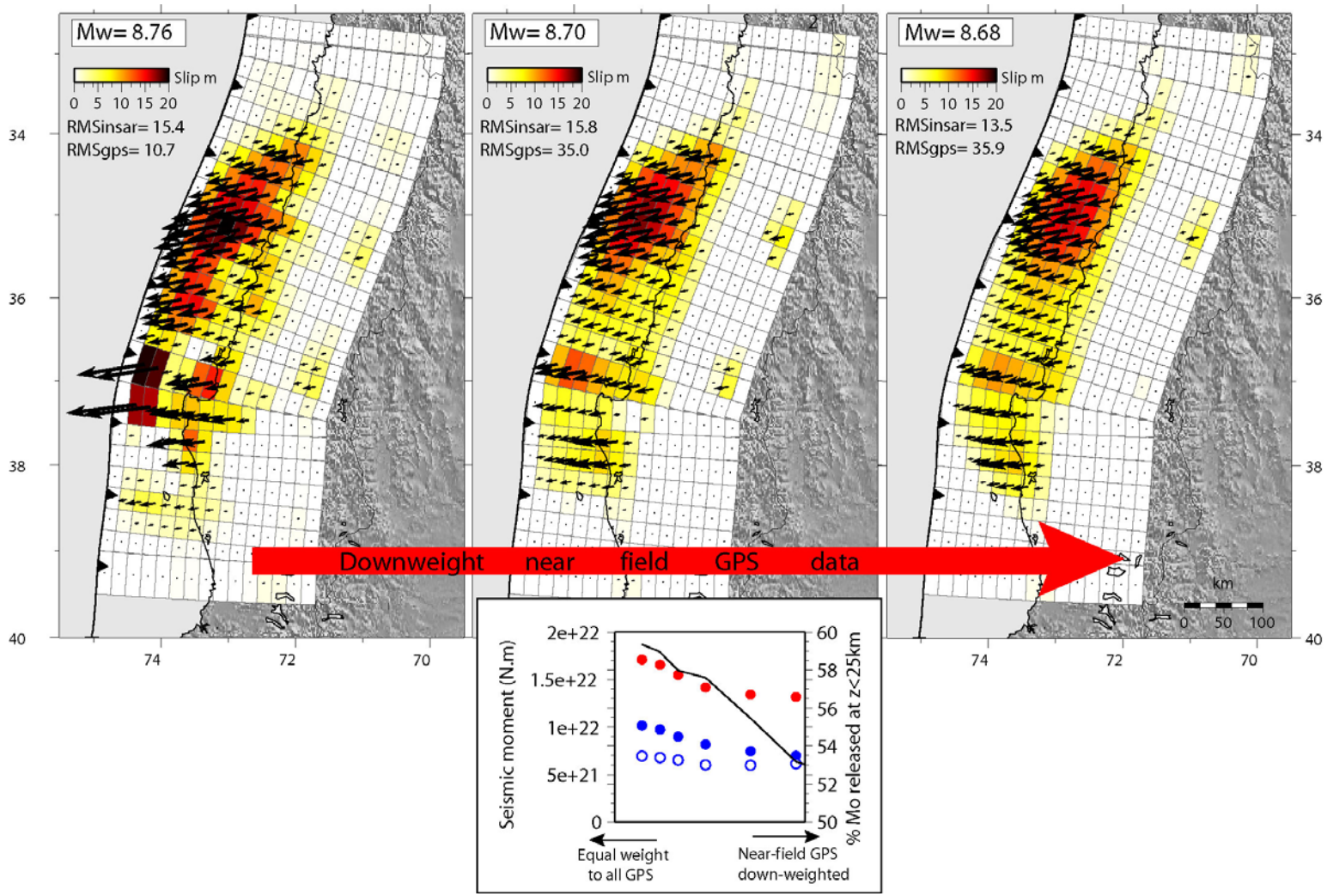

Fig. S14 Effect of down-weighting the near-field GPS data in the inversion. Left panel: Slip model obtained when weighting all GPS data equally in the inversion procedure. Middle and right panels: Slip models obtained when near-field GPS data have been increasingly down-weighted with respect to far-field GPS data. RMS residuals with respect to GPS and INSAR data are indicated in cm for each model. The bottom graph shows the decrease of the model total seismic moment (red dots) when near field GPS data are progressively down-weighted in the inversion. Blue dots show the decrease of the moment generated at shallow or large depths: full dots (depth < 25km) and open dots (depth > 25km). The black curve shows the percentage of seismic moment released at shallow depth (<25km). Models without near-field GPS data have less shallow slip and less slip between 35°S and 37°S.

Table S1: Co-seismic displacements (mm) for 27-Feb-2010 Maule, Chile Earthquake, cGPS data

Site	Position		Displacements			Uncertainties		
	Longitude	Latitude	Long	Lat	Vertical	Sigma lon	Sigma lat	Sigma up
IGS: International GNSS Service (http://igscb.jpl.nasa.gov)								
AREQ	-71,493	-16,466	2	-3	-9	4	2	10
BRAZ	-47,878	-15,947	1	-1	-1	1	1	4
GLPS	-90,304	-0,743	0	0	0	1	1	4
KOUR	-52,806	5,252	0	0	-1	1	1	4
LPGS	-57,932	-34,907	-18	-7	-2	4	2	13
RIO2	-67,751	-53,785	0	0	1	1	1	4
SANT	-70,669	-33,150	-250	-143	-24	4	2	9
RAMSAC: Argentinian cGPS network operated by Instituto Geografico Nacional (IGN) of Argentina (http://www.ign.gob.ar)								
ALUM	-66,597	-27,323	-1	-4	5	3	2	8
AZUL	-59,881	-36,767	-24	6	13	5	2	11
CATA	-65,774	-28,471	-8	-10	-5	5	2	12
MA01	-68,057	-38,951	-78	34	11	4	2	9
MZAE	-68,15	-33,255	-106	-34	21	4	2	10
MZAS	-68,335	-34,615	-211	-22	13	5	2	11
RWSN	-65,107	-43,299	-6	6	-12	8	3	29
SL01	-66,314	-33,156	-60	-22	5	4	2	9
SRLP	-64,28	-36,621	-49	1	21	5	2	14
TERO	-64,257	-27,789	-6	-6	-3	4	2	10
UCOR	-64,194	-31,435	-25	-9	15	4	2	10
UNRO	-60,628	-32,959	-15	-7	2	4	2	11
VBCA	-62,269	-38,701	-23	3	9	4	2	11
RBMC : Brasilian cGPS network operated by Instituto Brasileiro de Geografia e estatistica (IBGE) of Brasil (http://www.ibge.gov.br/)								
CHPI	-44,985	-22,687	-1	1	1	1	1	4
CUIB	-56,07	-15,555	-9	-3	-11	5	2	13
MABA	-49,122	-5,362	4	-6	31	7	2	18
MSCG	-54,541	-20,441	-5	-3	-1	5	2	13
NAUS	-60,055	-3,023	1	-2	-4	5	2	13
POAL	-51,12	-30,074	-5	0	10	4	2	10
POVE	-63,896	-8,709	-1	2	8	4	2	11
SAVO	-38,432	-12,939	4	4	-10	5	2	14
TOPL	-48,331	-10,171	-2	2	6	5	2	15
UFPR	-49,231	-25,448	-2	0	1	4	2	9
TIGO: Chilo-German observatory of Concepcion operated by BKG-Frankfurt/U-Concepcion/IGM (http://www.tigo.cl)								
CONZ	-73,025	-36,844	-2892	-690	-35	4	2	9
CAP - Andes GPS Project : South American network operated by Ohio State University/University of Memphis/University of Hawai								
ANTC	-71,532	-37,339	-761	171	-16	4	2	11
CFAG	-68,233	-31,602	-35	-17	11	4	2	9
COPO	-70,338	-27,385	-2	3	0	3	2	8
ESQU	-71,323	-42,917	-5	-4	4	4	2	9
LHCL	-65,595	-38,003	-59	17	7	4	2	9
MZAC	-68,876	-32,895	-109	-48	15	5	2	11

UNSJ	-68,577	-31,541	-29	-15	6	4	2	10
TUCU	-65,23	-26,843	-2	-4	6	5	2	14

LIA-MdB: Chilo-french cGPS network operated jointly by U-Chile and CNRS (https://www.lia-mb.net)

BTON	-71,487	-30,263	3	10	-2	4	2	9
CMBA	-70,999	-31,188	-7	7	-1	4	2	10
CNBA	-71,458	-31,398	-2	9	-3	4	2	10
CONS	-72,412	-35,331	-4696	-385	-367	3	2	8
CRZL	-71,41	-29,102	1	8	7	9	3	18
DGF1	-70,662	-33,457	-430	-199	-30	5	2	12
EMAT	-71,663	-31,147	-2	14	-9	4	2	10
JUNT	-70,094	-29,977	-1	4	-2	5	2	13
LSCH	-71,246	-29,908	0	8	-3	4	2	11
MAUL	-70,821	-35,810	-1047	126	5	4	2	9
OVLL	-71,204	-30,604	4	10	-4	4	2	11
PEDR	-70,689	-30,839	-3	1	-3	4	2	9
PFRJ	-71,635	-30,675	-1	12	-7	4	2	10
PORT	-70,13	-32,835	-133	-89	8	3	2	7
RCSD	-71,613	-33,654	-712	-345	-160	3	2	8
ROBL	-71,015	-32,976	-169	-113	-38	3	2	8
SILL	-70,739	-29,255	1	6	-3	3	2	8
SJAV	-71,733	-35,595	-2340	277	-451	6	3	14
TOLO	-70,806	-30,170	-4	9	0	4	2	10
VALL	-70,764	-28,572	-1	4	5	4	2	11
VALN	-71,635	-33,028	-104	-27	-52	6	3	15
VNEV	-70,249	-33,354	-292	-143	1	4	2	11

Table S2: Co-seismic displacements (mm) for 27-Feb-2010 Maule, Chile Earthquake, campaign data

Site	Position		Displacements			Uncertainties		
	Longitude	Latitude	Lon	Lat	Vertical	Sigma lon	Sigma lat	Sigma up
BAT0	-71,962	-35,307	-3347	102	-728	6	4	12
CAP0	-73,272	-37,245	-3379	-591	808	35	19	54
CHL0	-72,205	-36,639	-1896	74	-388	10	5	20
CLM0	-72,812	-36,236	-3488	-668	412	10	5	16
CLP0	-71,625	-37,336	-921	180	-53	6	4	13
CO10	-72,415	-35,318	-4858	-438	-285	9	5	14
CO20	-72,491	-35,412	-4628	-341	-59	10	6	18
CO31	-72,519	-35,493	-4308	-335	158	14	7	24
CO40	-72,626	-35,586	-4234	-522	568	9	5	16
CO60	-72,606	-35,828	-3426	-525	228	6	4	11
CO70	-72,639	-35,843	-3505	-607	448	10	6	17
CO80	-72,744	-35,949	-3730	-805	555	11	6	19
COLB	-71,347	-35,677	-1743	249	-102	6	4	10
CT20	-72,255	-35,464	-3678	-58	-587	10	6	18
CT30	-72,086	-35,558	-3116	103	-716	8	5	15
CT60	-71,069	-35,709	-1382	191	99	6	4	11
CT70	-70,834	-35,815	-1124	199	102	9	4	14
CT80	-70,399	-35,991	-713	164	66	110	8	102
LAJ0	-72,697	-37,255	-2300	-11	-507	30	17	36
LLA0	-71,344	-37,369	-765	169	120	6	4	13
LLI0	-73,569	-37,192	-4879	-434	1748	34	19	49
LTA0	-73,142	-37,059	-2717	-608	438	10	6	18
MRC0	-71,955	-37,411	-1172	168	-37	6	4	12
NIN0	-72,437	-36,410	-2336	-212	-299	6	5	11
PTU0	-72,269	-35,172	-4777	-505	-373	8	5	14
PUL0	-72,942	-37,285	-2663	-204	-296	30	18	36
QLA0	-72,125	-36,085	-2395	145	-577	6	4	10
RAQ0	-73,436	-37,256	-3922	-504	1452	34	19	49
RUM0	-73,613	-37,176	-5029	-529	---	7	5	---
SGE0	-72,231	-37,393	-1575	209	-233	30	18	42
SLT0	-72,384	-37,216	-1919	123	-306	29	17	36
TETS	-73,193	-36,773	-3296	-789	693	18	14	40

Table S3: 12-day post-seismic horizontal displacements (mm) for 27-Feb-2010 Maule, Chile Earthquake, cGPS data

Site	Position		Displacements		Uncertainties	
	Longitude	Latitude	Long	Lat	Sigma lon	Sigma lat
ALUM	293,403	-27,323	-4	-3	3	2
AREQ	288,507	-16,466	-3	-2	4	2
AZUL	300,119	-36,767	-1	-7	5	3
BTON	288,513	-30,263	-3	4	4	2
CATA	294,226	-28,471	-1	1	5	2
CFAG	291,767	-31,602	-4	-5	4	2
CHPI	315,015	-22,687	1	-1	1	1
CMBA	289,001	-31,188	-1	2	4	2
CONS	287,588	-35,331	-69	-8	3	2
CONZ	286,975	-36,844	-145	7	4	2
COPO	289,662	-27,385	0	2	3	2
CRZL	288,590	-29,102	-1	0	9	3
CUIB	303,930	-15,555	13	-5	5	2
DGF1	289,338	-33,457	-30	-10	5	2
EMAT	288,337	-31,147	2	4	4	2
ESQU	288,677	-42,917	-4	-3	4	2
GLPS	269,696	-0,743	1	0	1	1
JUNT	289,906	-29,977	-1	0	5	2
KOUR	307,194	5,252	0	-1	1	1
LHCL	294,405	-38,003	-10	0	4	2
LPGS	302,068	-34,907	-10	1	5	2
LSCH	288,754	-29,908	0	1	4	2
MABA	310,878	-5,362	-11	7	8	3
MAUL	289,179	-35,810	-99	17	3	2
MSCG	305,459	-20,441	3	0	5	2
MZAC	291,124	-32,895	-9	-3	5	2
MZAE	291,850	-33,255	-9	-12	4	2
MZAS	291,665	-34,615	-12	-7	5	2
NAUS	299,945	-3,023	0	1	5	2
OVLL	288,796	-30,604	-2	3	4	2
PEDR	289,311	-30,839	0	5	4	2
PFRJ	288,365	-30,675	2	3	4	2
POAL	308,880	-30,074	-1	-6	5	2
PORT	289,870	-32,835	-6	-10	3	2
POVE	296,104	-8,709	0	0	5	2
RCSD	288,387	-33,654	-60	0	3	2
RIO2	292,249	-53,785	0	1	1	1
ROBL	288,985	-32,976	-11	-1	3	2
RWSN	294,893	-43,299	-21	-1	12	4
SANT	289,331	-33,150	-18	-5	4	2
SAVO	321,568	-12,939	-5	6	5	2
SILL	289,261	-29,255	-2	2	3	2
SL01	293,686	-33,156	-9	-1	4	2
SRLP	295,720	-36,621	-9	-3	5	2
TERO	295,743	-27,789	-2	1	4	2
TOLO	289,194	-30,170	-2	1	4	2
TOPL	311,669	-10,171	-2	-4	5	2
TUCU	294,770	-26,843	-6	4	5	2
UCOR	295,806	-31,435	32	-6	15	3

UFPR	310,769	-25,448	-4	-2	4	2
UNRO	299,372	-32,959	-11	-7	4	2
UNSJ	291,423	-31,541	-7	-5	4	2
VALL	289,236	-28,572	-1	2	4	2
VALN	288,365	-33,028	-9	2	6	3
VBCA	297,731	-38,701	-10	-1	4	2
VNEV	289,751	-33,354	-22	-17	4	2

Table S4 Comparison between several published slip distribution models of the February 27, 2010 Mw 8.8 Maule Earthquake. We calculated the fit between the displacements computed from those models and our GPS observations (horizontal and vertical components). Mean residuals are given in cm. Slip models, observed, computed and O.-C. residual-vectors are given in figures S6 to S13.

Type of data [(reference)]	Horizontal mean res.	Vertical mean res.	Figure
GSN broadband waveforms [33]	75.7	33.0	Fig. S6
Teleseismic and far-field cGPS [34]	170.0	35.1	Fig. S7
Teleseismic body waves and LP Surface waves [35]	95.0	63.0	Fig. S8
Teleseismic P and SH observations [18]	94.0	28.0	Fig. S9
Far-field cGPS, INSAR and teleseismic data [19]	50.0	32.0	Fig. S10
INSAR, and far field cGPS [16]	32.9	29.3	Fig. S11
cGPS, INSAR and seismic data [20]	52.4	24.5	Fig. S12
Survey GPS, near-field and far-field cGPS, INSAR and land level variation [(this work)]	16.3	10.7	Fig. S13

References and Notes

1. R. Bilham, *Science* **308**, 1126 (2005).
2. C. Vigny *et al*. *Nature* **436**, 201 (2005).
3. C. Darwin, *Journal of Researches into the Natural History and Geology of the Countries Visited During the Voyage of the H.M.S. Beagle Round the World* (John Murray, London, 1876).
4. R. FitzRoy, "Narrative of the surveying voyages of His Majesty's Ships Adventure and Beagle between the years 1826 and 1836, describing their examination of the southern shores of South America, and the Beagle's circumnavigation of the globe" (1839).
5. F. Montessus de Ballore, *Historia Sısmica de los Andes Meridionales, 6 vols.* (Editorial Cervantes, Santiago de Chile, 1916).
6. C. Lomnitz, Grandes terramotos y tsunamis en Chile durante el periodo 1535-1955, *Geofis. Panamericana* **1**, 151 (1971).
7. S. L. Beck, S. Barrientos, E. Kausel, M. Reyes, *J. S. Am. Earth. Sci*. **11**, 115 (1998).
8. R. Madariaga, M. Métois, C. Vigny, J. Campos, *Science* **328**, 181 (2010).
9. S. Nishenko, *J. Geophys. Res.* **90**, 3589 (1985).
10. Z. Altamimi, X. Collilieux, J. Legrand, B. Garayt, C. Boucher, *J. Geophys. Res*. **112**, B09401 (2007).
11. J. Campos *et al*., *Phys. Earth Planet. Int.* **132**, 177 (2002).
12. J. C. Ruegg *et al*., *Geophys. Res. Lett.* **29(**11), 10.1029/2001GL013438 (2002).
13. J. C. Ruegg *et al*., *PEPI*, 10.1016/j.pepi.2008.02.015 (2009)
14. Materials and methods are available as supporting material on *Science* Online.
15. M. Farías *et al*., *Science* **329**, 916 (2010).
16. X. Tong *et al*., *Geophys. Res. Lett*. **37**, L24311, doi:10.1029/2010GL045805 (2010).
17. M. Moreno, M. Rosenau, O. Oncken., *Nature* **467**, 198 (2010).
18. T. Lay *et al*., *Geophys. Res. Lett*. **37**, L13301, doi:10.1029/2010GL043379 (2010).
19. B. Delouis, J.-M. Nocquet, M. Vallée, *Geophys. Res. Lett*. **37**, L17305, doi:10.1029/2010GL043899 (2010).

20. S. Lorito *et al*., *Nat. Geosci.* **4**, 173 (2011).

21. R. D. Hyndman, M. Yamano, D. A. Oleskevich, *Island Arc* **6**, 244, (1997).

22. T. Tanimoto, C. Ji, *Geophys. Res. Lett*. **37**, L22312 (2010).

23. M. Béjar-Pizarro, D. Carrizo, A. Socquet, R. Armijo, and the North Chile Geodetic Team, *Geophys. Jour. Int*., doi 10.1111/j.1365-246X.2010.04748.x (2010).

24. R. W. King, Y. Bock, Mass. Inst. of Technol., Cambridge (2000).

25. T. A. Herring *et al*., *J. Geophys. Res.* ***95***, 12561 (1990).

26. J. M. Dow, R. E. Neilan, G. Gendt, *Adv. Space Res.* **36**, 320, 2005.

27. K. Larson, P. Bodin, J. Gomberg, *Science* **300**, 1421 (2003).

28. G. Emore *et al*., *Bull. Seismol. Soc. Am*. **97**, 357 (2007).

29. R. Smalley, *Seismol. Res. Lett*. **80**, 1054 (2009).

30. Y. Okada, *Bull. Seismol. Soc. Am.* **75**, 1135 (1985).

31. O. Coutant, Programme de simulation numérique AXITRA, Rapport LGIT-Université J. Fourier, Grenoble, France (1990).

32. M. Bohm *et al*., *Tectonophysics* **356**, 275 (2002).

33. G. Hayes, Preliminary SZGC results, near coast of central Chile (2010); http://earthquake.usgs.gov/earthquakes/eqinthenews/2010/us2010tfan/finite_fault.php

34. A. Sladen, S. Owen, Preliminary model combining teleseismic and GPS data 02/27/2010 (M_w 8.8), Chile, (2010); www.tectonics.caltech.edu/slip_history/2010_chile/prelim_gps.html

35. G. Shao, X. Li, Q. Liu, X. Zhao, T. Yano, C. Ji, UCSB, Preliminary slip model of the Feb 27, 2010 M_w 8.9 Maule, Chile Earthquake (2010); www.geol.ucsb.edu/faculty/ji/big_earthquakes/2010/02/27/chile_2_27.html